Extraction of mobile charge carrier photogeneration yield spectrum of ultrathin film metal oxide photoanodes for solar water splitting

Daniel A Grave[1,2*+], David S. Ellis[1+], Yifat Piekner[3+], Moritz Kölbach[4], Hen Dotan[1], Asaf Kay[1], Patrick Schnell[4], Roel van de Krol[4], Fatwa F. Abdi[4], Dennis Friedrich[4], Avner Rothschild[1]*

[1]Department of Materials Science and Engineering, Technion – Israel Institute of Technology, Haifa, Israel
[2]Department of Materials Engineering and Ilse Katz Institute for Nanoscale Science and Technology, Ben Gurion University of the Negev, Be'er Sheva, Israel
[3]The Nancy & Stephen Grand Technion Energy Program (GTEP), Technion – Israel Institute of Technology, Haifa 32000, Israel
[4]Institute for Solar Fuels, Helmholtz-Zentrum Berlin für Materialien und Energie GmbH, Berlin, Germany

*Email: dgrave@bgu.ac.il, avnerrot@technion.ac.il

+equal contribution

Abstract

Light absorption in semiconductor photoabsorbers can excite electrons and holes into a variety of different states. Some of these excitations yield mobile charge carriers, whereas others result in localized excited states that cannot contribute to photocurrent. The photogeneration yield spectrum, $\xi(\lambda)$, represents the wavelength-dependent ratio between the contributing absorption that ultimately generates mobile charge carriers and the overall absorption. Despite being a vital material property, it is not trivial to characterize. We present an empirical method to extract $\xi(\lambda)$ through optical and external quantum efficiency measurements of ultrathin films. We apply this method to hematite photoanodes for water photo-oxidation, and demonstrate that it is self-consistent for different illumination conditions and applied potentials. We show agreement between the extracted $\xi(\lambda)$ spectrum and the photoconductivity spectrum measured by time-resolved microwave conductivity. These measurements reveal that mobile charge carrier

generation increases with increasing energy across hematite's absorption spectrum. Low energy non-contributing absorption fundamentally limits the conversion efficiency of hematite photoanodes and provides an upper limit to the achievable photocurrent that is substantially lower than that predicted based solely on absorption above the band gap. We extend our analysis to TiO_2 and $BiVO_4$ photoanodes, demonstrating the broader utility of the method for determining $\xi(\lambda)$.

Manuscript

At the heart of any semiconductor photoabsorber material in photovoltaic and photoelectrochemical cells for solar energy conversion is the ability to absorb light and thereby generate excess mobile charge carriers (electrons and holes) that give rise to photocurrent and photovoltage.[1] Many new photoabsorber materials have intricate and complex electronic and optical properties, to the effect that light can excite electrons and holes into a variety of different states. While some of these optically excited states are or can eventually become mobile charge carriers, others are stationary and cannot contribute to photocurrent. These non-contributing absorption processes include ligand field ($d \rightarrow d$) excitations which can be optically allowed by distortions from inversion symmetry and many body effects.[2,3] Likewise, organic photovoltaic materials also have different types of photoexcitations and excitons which have direct impact on the photocurrent.[4,5] The various types of optical excitations, contributing and non-contributing ones, could overlap in wavelength across the material's absorption spectrum. The wavelength-dependent ratio between the contributing and overall absorption defines the photogeneration yield spectrum $\xi(\lambda)$, equivalent to the probability of an absorbed photon of wavelength λ to ultimately generate a mobile charge carrier. This quantity is therefore of core importance for the development of photovoltaic and photoelectrochemical devices. However, $\xi(\lambda)$ can be difficult to properly characterize, because most of the pertinent measurements can only detect the photocurrent action

spectrum $J_{ph}(\lambda)$, which is comprised of many different optical and electronic factors. An intermingling of the inherent material properties (e.g. absorption processes and cross-sections, electronic transport and recombination mechanisms in bulk and through surface, optical constants), and the more macroscopic-level, adjustable properties (e.g. lengths and interfaces) of the device tested, are all factors which combine to produce $J_{ph}(\lambda)$ for the particular device. It is therefore desirable, as a basic measure, to characterize the system by only a few basic parameters, including $\xi(\lambda)$, which have straightforward physical definitions.

Here we present a method for extracting $\xi(\lambda)$ empirically, without any *a priori* assumptions about its shape. The derivation begins from a spatial collection efficiency model,[6,7] but using ultrathin films to remove all the spatial effects, thereby greatly simplifying the computation and avoiding *a priori* assumptions. As a case study, we first apply this method to study hematite (α-Fe_2O_3) photoanodes for water photo-oxidation in photoelectrochemical (PEC) cells for solar water splitting.[8] The results are compared with photoconductivity measurements using an entirely different, non-contact technique: time-resolved microwave photoconductivity (TRMC), whose action spectrum should, in principle, also be proportional to $\xi(\lambda)$, if the charge carrier mobility is wavelength independent.[9] Consistent with this prediction, the shape of the extracted $\xi(\lambda)$ and TRMC action spectrum were found to be similar. The consistency between these two diverse techniques, one an entirely D.C. method in a photoelectrochemical cell under applied bias, the other a totally non-contact method at microwave frequencies, demonstrates that both methods probe the same fundamental material property, and affirms that, in addition to being a guide for accurate device characterization, modelling and design, they provide invaluable insight into the material's inherent light absorption processes.

A standard measure of photovoltaic or photoelectrochemical device performance is the photocurrent action spectrum $J_{ph}(\lambda)$, normalized by the incident light spectrum, known as external quantum efficiency (EQE, synonymous with incident photon to electron conversion efficiency, IPCE).[10,11] For hematite, it was long noticed that its EQE falls off with increasing wavelength, at a rate beyond what would be expected from the decreasing optical absorption.[12] This observed discrepancy has been common to all hematite photoanodes, even when considering spatial effects of where the light is absorbed in the sample.[13] Different interpretations have been hypothesized to describe this phenomenon, and are still under debate. The first was suggested by Kennedy and Frese, who attributed the wavelength-dependent photocurrent action spectrum to the existence of multiple absorption bands, only one of which generates mobile charge carriers that contribute to the photocurrent, thereby resulting in a less than unity value of $\xi(\lambda)$ at different wavelengths.[12] More recently, this notion of differentiating between the contributions of holes excited at different wavelengths was revived by a few reports,[14,15] and a similar suggestion has been given by Hayes et al., with assignment of the absorption spectrum to a combination of overlapping ligand-to-metal charge transfer (LMCT) and ligand field excitations.[3] Consistent with this general picture, Braun et al. found evidence in the X-ray absorption spectrum of oxygen for the generation of two kinds of holes in hematite under illumination.[16] An alternative explanation for the wavelength dependence, based on interpretation of ultrafast extreme ultraviolet (XUV) spectroscopy, has been recently suggested by Carneiro et al.[17] In their model, higher energy excitation results in photogenerated polaronic charge carriers with larger mobility and longer lifetimes. In light of these intriguing reports, there is a clear need for spectrally resolved characterization of how optical absorption mechanisms affect mobile charge carrier yield in complex materials such as hematite, where absorption of above bandgap photons do not necessarily produce free electrons and holes

as they do in conventional photoabsorber materials such as silicon. Herein we develop an empirical method for accurate determination of the spectral profile of ξ(λ) for hematite as a case study, followed by TiO_2 and $BiVO_4$ as additional examples, and together with complementary observations from TRMC, demonstrate its value towards understanding the nature of optical absorption mechanisms and charge carrier generation, and for re-evaluating fundamental device limits.

We derive the empirical extraction of ξ(λ) from a one-dimensional spatial collection efficiency model, which has been used to deduce the probability $p(x)$ of a charge carrier generated at distance x from the surface, to reach and make it across the surface at x=0 without recombining.[6,7,18] It uses the measured EQE spectrum combined with measured optical properties of the device, without any *a priori* assumptions. The EQE spectrum can be constructed by the following integral over the photoabsorber layer thickness d:

$$EQE(\lambda) = \int_0^d \frac{I(\lambda,x)}{I_0(\lambda)} \cdot \alpha(\lambda) \cdot \xi(\lambda) \cdot p(x) \cdot \mathrm{d}x \qquad (1)$$

where $I(\lambda,x)$ is the wavelength-dependent photon flux at point x, normalized by the incident flux $I_0(\lambda)$ at the surface (x=0), and $\alpha(\lambda)$ is the optical absorption coefficient of the photoabsorber layer. In Equation (1), the product $I(\lambda,x) \cdot \alpha(\lambda) \cdot \xi(\lambda)$ describes the mobile charge carrier generation, while charge transport and recombination effects are contained in $p(x)$ which is assumed to be wavelength-independent. This assumption is supported by previous TRMC measurements which show that the charge carrier lifetimes do not change with excitation wavelength in hematite.[9] Similar conclusions have been found for other photoabsorber materials.[19] The analysis takes into account that the depth of optical penetration is wavelength-dependent, which has significant impact on the photocurrent spectra when the mean minority charge carrier collection length is less

than the thickness of the photoabsorber layer. Experimentally, EQE(λ) is directly measured, while $I(\lambda,x)$ and $\alpha(\lambda)$ can be extracted from spectroscopic ellipsometry.[20,21] The remaining unknowns, $\xi(\lambda)$ and $p(x)$, are to be solved for, typically numerically.[7] For conventional photoabsorber materials like silicon, where $\xi(\lambda) = 1$ throughout the absorption spectrum, this method has been applied successfully to obtain $p(x)$,[6] and most prior analyses have indeed neglected $\xi(\lambda)$.[6,22,23] A similar approach was also adopted recently for complex metal oxide photoabsorbers such as copper vanadate[24] and for colloidal quantum dot solar cells.[25] For non-trivial, unknown $\xi(\lambda)$, as is the case for some photoabsorber materials such as hematite, it can be a daunting task to solve Equation (1), requiring several numerical steps and *a priori* assumptions.[7] This task falls in the category of ill-posed inverse problems, which may have multiple solutions, of which only one is the correct physical solution.[23] However, if the layer thickness (d) is small compared to the length-scale of the spatial variation in both $I(\lambda, x)$ and $p(x)$, then all of the spatial variations can be replaced by their respective spatially averaged values, $\bar{I}(\lambda)$ and $\bar{p}$. A detailed analysis of the error introduced by this approximation is given in the Supplementary Information. Under those conditions, Equation (1) can be simplified as a product of averages and explicitly solved for $\xi(\lambda)$:

$$\xi(\lambda) \cong \lim_{d\to 0}\left\{\frac{EQE(\lambda)}{\alpha(\lambda)\cdot d}\right\}\cdot\frac{1}{\frac{\bar{I}(\lambda)}{I_0(\lambda)}\cdot\bar{p}} \qquad (2)$$

For highest accuracy $\bar{I}(\lambda)$ would ideally be obtained from optical modelling, such as from spectroscopic ellipsometry or other methods appropriate to the optical stack.[26] These methods would allow one to accurately account for effects such as multiple reflections and parasitic absorption in other layers, which could have a profound effect on the results. However, if a sufficiently accurate optical model is not available, a crude approximation would be that most of the optical losses in the limit of small d ($d << \alpha^{-1}$) come from interface reflection, and therefore,

$\lim_{d\to 0} \frac{\bar{I}(\lambda)}{I_0(\lambda)} \approx 1 - R(\lambda)$, where R is the reflectance. With this latter substitution, Equation (2) resembles the classical equation for internal quantum efficiency (IQE), divided by a $\bar{p}$ factor, which also becomes evident by equating $\alpha \cdot d \cdot (\bar{I}/I_0)$ in the denominator of Equation (2) with the absorptance. We emphasize that only absorption in the photoabsorber layer should be considered. Improper accounting for absorption in each layer in the optical stack (comprising a substrate, current collector, photoabsorber, and possibly other layers) whereby light absorbed in non-contributing layers is erroneously included in the calculation can adversely affect the analysis accuracy. Additionally, if the thickness d of the photoabsorber layer becomes comparable to the length scale of variations of $p(x)$ and $I(\lambda,x)$, the resultant $\xi(\lambda)$ spectrum from the "IQE-like" approximation (Equation 2) will be distorted by spatial $p(x)$ effects. Previous works emphasized the importance of correct optical modelling using the transfer matrix method,[18,20,26] however $\xi(\lambda)$ itself was not accounted for, which we demonstrate below to be a significant effect in the case of hematite. Finally, it is important that the electrolyte solution is taken into account in the optical model, as it can significantly affect the reflection and absorptance in the photoabsorber during the EQE measurement.

To ensure the validity of the small d condition for Equation (2) in our case study, we simulated different thicknesses to see how it affects the error in the approximation, presented in the Supplementary Information (Figures S2 and S3). The simulations show that hematite films of thickness less than 10 nm would be required to keep the error down to a few percent. Therefore, a 7 nm thick film of Sn-doped hematite was deposited using pulsed laser deposition (PLD) on an indium-tin-oxide (ITO) coated glass substrate. Spectroscopic ellipsometry was used to extract the optical constants of the ITO and hematite layers in the stack in order to create an accurate optical model for light absorption in the sample. The thicknesses of the films extracted from cross-section

transmission electron microscopy (TEM) were used to guide the optical modelling. It has been reported that for film thicknesses under ~20 nm, the optical spectra of hematite thin films may be affected due to structural or quantum size effects.[27,28] Consistent with these previous observations, the absorption coefficient of the 7 nm thick hematite film shows a blueshift of the main near-UV peak, as well as an apparent suppression of the ~550 nm feature, relative to that of a 150 nm thick hematite film as shown in Figure S9. To validate the extracted optical constants, transmission and reflection measurements were performed with a spectrophotometer, and compared to optical simulations using the transfer matrix method with the model's optical parameters. Figure 1(a) shows excellent agreement over a wide wavelength range between the model simulations and transmittance (T) and reflectance (R) measurements. In the figure, the total absorptance, i.e., the total fraction of absorbed photons in the sample out of the incident photon flux ($F_A = 1 - R - T$), is also plotted along with the absorptance only in the hematite film, $A_{hematite} = \alpha \cdot d \cdot (\bar{I}/I_0)$. The difference between the absorptance of the full stack (green curve in Figure 1(a)) and hematite layer (black curve), highlights the importance of accounting for parasitic absorption in the ITO current collector and glass substrate in the optical model, and it follows that spectrophotometer measurements alone may not be sufficient for the analysis. Similar optical analysis was performed for back-illumination, and is presented in Figure S1.

Photoelectrochemical EQE measurements[11] were performed with a custom system that can measure EQE(λ) with low noise under a light bias from a white LED source at approximately one sun intensity (described in detail in the Methods, and Supplementary Information). Figure 1(b) shows the EQE spectra for the cases of the wavelength-varying probe light incident on the front or back side, while maintaining the same white light bias conditions on the front of the sample. We note that the monochromatic probe light is typically 100 times weaker than the LED bias, so

sample conditions such as surface band-bending are maintained solely by the potential and LED bias irrespective of whether the probe light is applied to the front or back of the sample. Also shown in Figure 1(b) are the respective absorptance spectra in the hematite layer calculated with the inclusion of the electrolyte layer, which has a different index of refraction than air, in the optical model. Significant differences are apparent between front and back illumination for both the hematite layer absorptance and EQE spectra. Applying both sets of data to Equation (2) resulted in respective spectra of $\bar{p} \cdot \xi(\lambda)$ which are presented in Figure 1(c). We emphasize that these come directly from the EQE measurements and optical model calculations (that are supported by spectroscopic ellipsometry and spectrophotometry measurements), without any offsets or scaling. Since the applied potential and light bias conditions on the sample are the same for both cases, the average charge carrier collection probability $\bar{p}$ should be unchanged.

Since the value of $\bar{p}$ is unknown, we cannot extract the absolute magnitude of $\xi(\lambda)$, but we can extract its spectral profile. The consistency of the $\bar{p} \cdot \xi(\lambda)$ spectra resulting from the rather diverse datasets of front and back illumination validates our approach, and verifies that the 7 nm hematite film meets the requirement for applicability of Equation (2). The differences between these two derived spectra can be considered as a gauge of the error in the analysis. We note some similarity of the $\xi(\lambda)$ spectra in Figure 1(c) to IQE spectra measured in hematite thin films[29] and nanostructures.[30] Nanostructured porous layers where lateral charge collection dominates[8] can have a considerably relaxed thickness requirement for estimating $\xi(\lambda)$, but require increased complexity of optical modelling as compared to dense ultrathin films. Changing the applied potential had very little effect on the EQE shape, as described in the Supplementary Information. Shown in Figure S4(d), only a small change in the ~400 nm peak height is observed, even as the value of EQE decreased by 3 orders of magnitude. It follows that $\xi(\lambda)$ is likewise independent of

the applied potential, unless the absorptance significantly changes its spectral shape but EQE does not. Previous spectro-photoelectrochemical studies of hematite photoanodes showed that the steady-state absorptance at a wavelength of ~580 nm changes by only ~20 mOD when applying potential of 1.6 V vs. the reversible hydrogen electrode (RHE) scale (V_{RHE}), which would have a negligible effect on $\xi(\lambda)$.[31] This implies that the applied potential only affects $p(x)$, presumably through $p(0)$ at x=0, which is the potential-dependent charge transfer efficiency at the surface, and it is independent of the photoexcitation wavelength. That the EQE spectral shape does not change by changing $p(x)$ gives some credence to the premise that $p(x)$ is independent of wavelength for the hematite film. This is consistent with the wavelength-independent lifetimes of photogenerated charge carriers measured by TRMC in reference [9] and presented below. Wavelength independence of photogenerated hole behavior at the surface was also confirmed by transient photocurrent vs. surface charge measurements.[14]

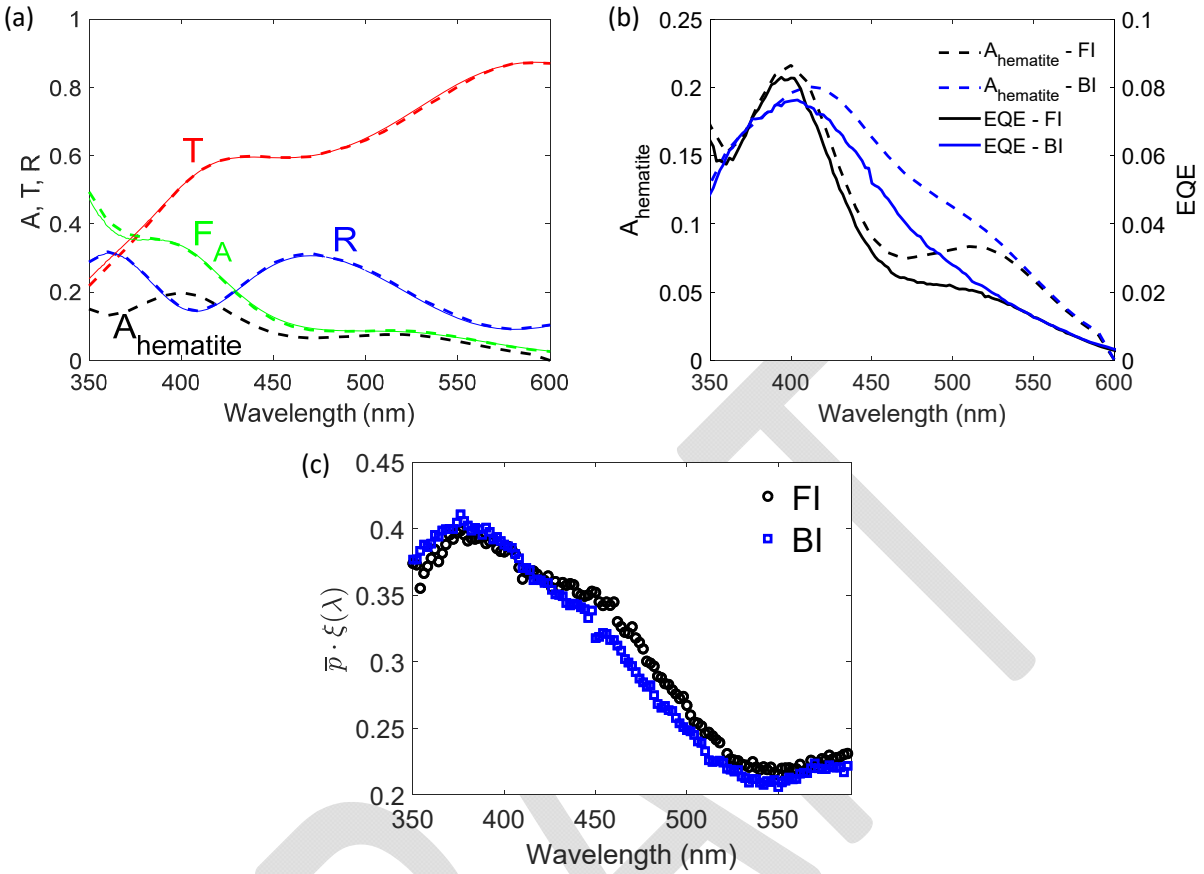

Figure 1. Extraction of the photogeneration yield spectrum from optical and photoelectrochemical EQE measurements of a 7 nm thick hematite film. (a) Measured (solid line) and calculated (dashed line) transmittance (red), reflectance (blue) and absorptance (green) spectra in front illumination in air. The black dotted line is the calculated absorptance in the hematite layer only. (b) The calculated hematite absorptance spectra in water (dashed lines) and EQE spectra measured at 1.6 V_{RHE} (solid lines) in front (black) and back (blue) illumination (FI and BI). (c) The extracted $\bar{p} \cdot \xi(\lambda)$ spectra for front (black) and back (blue) illumination.

While accurate extraction of $\xi(\lambda)$ (to a factor of a constant $\bar{p}$) was demonstrated above for an ultrathin hematite film, one might ask whether this spectrum is indicative of $\xi(\lambda)$ for a thicker hematite film given the possibility of quantum confinement effects in ultrathin films.[27,28] It would therefore be useful to compare with another measurement technique that nominally measures a similar quantity to $\xi(\lambda)$, but that does not require ultrathin films where quantum confinement could

be prevalent. One such method is TRMC, a contactless pump-probe technique where the sample is placed in a microwave cavity, and excited by a nanosecond laser pulse.[9,32] The resulting transient photoconductivity, $\Delta\sigma(t)$, in the sample is probed by monitoring light-induced changes in the cavity's reflected microwave power, $\frac{\Delta P}{P}(t)$, described by the following relation:

$$\frac{\Delta P}{P}(t) = -K \cdot \Delta\sigma(t) \qquad (3)$$

where *K* is the sensitivity factor which depends on resonance characteristics and properties of the cavity and sample.[33] The ratio between the amount of mobile charge carriers probed by the microwave and the absorbed photon fluence, is defined as the quantum yield, $\phi(\lambda)$. We note that $\phi(\lambda)$ is essentially equivalent, in principle, to the previously defined photogeneration yield, $\xi(\lambda)$. Supporting this notion, previous studies on organic semiconductor materials have suggested a link between the IQE measured in photovoltaic devices with the photogenerated charge carrier yield probed by TRMC.[34,35] The product of $\phi(\lambda)$ and the sum of the electron and hole mobilities $\sum \mu = \mu_e + \mu_h$, (or $\phi \sum \mu$ for brevity), can be related to the change in peak photoconductivity prior to recombination, $\Delta\sigma_{max}$ extracted from the TRMC measurement by:[32]

$$\phi(\lambda) \sum \mu = \frac{\Delta\sigma_{max}(\lambda)}{eI_0(\lambda) \cdot F_A(\lambda)/d} \qquad (4)$$

where $I_0(\lambda)$ is the number of incident photons per cm^2 per pulse, and *e* is the elementary charge. As TRMC measurements are made in air on transparent substrates (sapphire in our case) without parasitically absorbing current collectors, we can approximate that the total absorptance F_A is equal to the absorptance in the hematite film, $A_{hematite}$. Equation (4) expresses that the product of quantum yield and mobility sum can be presented as photoconductivity normalized by the product of the elementary charge and average density of absorbed photons, e· $I_0(\lambda) \cdot F_A(\lambda)/d$. However,

due to experimental uncertainty in the quantification of K, which is excitation wavelength independent, and since we are interested in the spectral or temporal shapes, we present our results in arbitrary units, noting that $\phi(\lambda)\sum\mu$ is proportional to $\frac{\Delta\sigma_{max}(\lambda)}{I_0(\lambda)\cdot F_A(\lambda)}$.

TRMC measurements were performed on an epitaxial 150 nm thick (0001) oriented Sn-doped hematite film deposited on *c*-plane sapphire. Measurements were made at various wavelengths across hematite's absorption spectrum (from 405 to 590 nm) in increments of 5 nm. Given the intensity dependence of the TRMC signal as discussed in the Supplementary Information and shown in Figure S5, neutral density filters were selected to keep the absorbed photon fluence as constant as possible (between 6×10^{13} and 8×10^{13} photons / pulse / cm^2) over the wavelength range measured. The transient photoconductivity response for selected wavelengths is plotted in Figure 2(a).

As can be seen, $\Delta\sigma_{max}/(F_A*I_0)$, proportional to $\phi\sum\mu$, varies significantly with excitation wavelength, suggesting that either ϕ or $\sum\mu$ (or both) vary with wavelength. Since the TRMC measurement cannot directly distinguish the variables within the $\phi\sum\mu$ product, it is non-trivial to determine which of either quantum yield or effective mobility is responsible for the wavelength dependence. However, a closer look at the charge carrier decay dynamics provides a compelling indication. Figure 2(b) shows that when the transient photoconductivity is normalized to its peak value, the decay dynamics are identical for different excitation wavelengths on the nanosecond time scale of our TRMC experiments. The transients were fit to a bi-exponentially decaying function as described in the Supplementary Information, and the fitted time constant of the fast decay was determined to be 30 ± 3 ns across the entire wavelength range. This indicates that the TRMC measurements probe mobile charge carriers with the same dynamics throughout the entire

wavelength range, implying that the wavelength dependence of the TRMC response likely originates from variation in the quantum yield (ϕ) rather than a change in the mobilities ($\sum \mu$),[19] and that the photo-excited charge carrier mobilities are independent of excitation wavelength. Various processes have recently been proposed to occur over fast time-scales during photoexcitation, such as self-heating[3] or formation of polarons,[17] which are potentially relevant and should not be overlooked in relation to the present analysis. We briefly review these processes in the Supplementary Information, and present arguments that heat dissipation is not responsible for the TRMC signal, and can instead be attributed to polaronic charge transport. The formation of polarons following photoexcitation was concluded to occur on a timescale of a few ps from ultrafast THz photoconductivity,[9] XUV spectroscopy,[17] and most recently "pump-push" photocurrent measurements.[36] The lifetime of these polaronic charge carriers has been suggested to be on the order of ns and longer,[36] consistent with the present results.

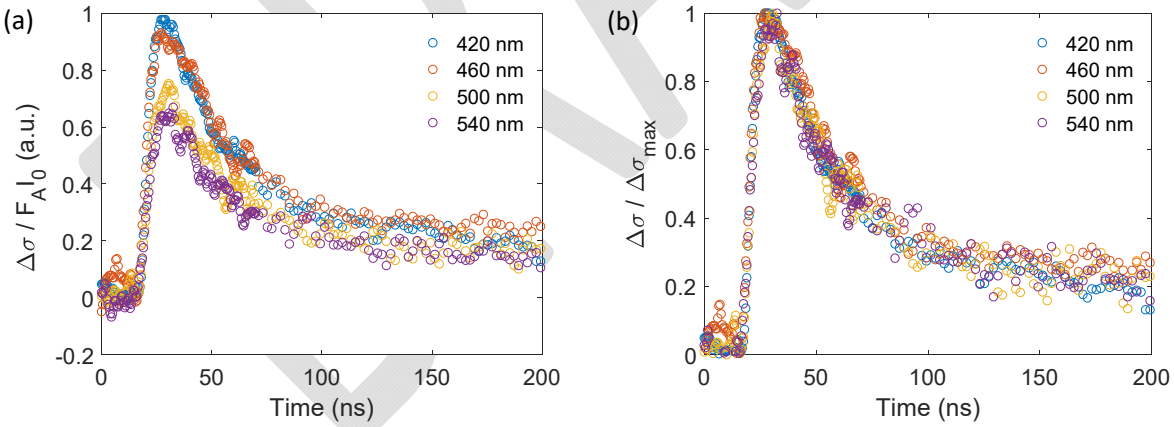

(c)

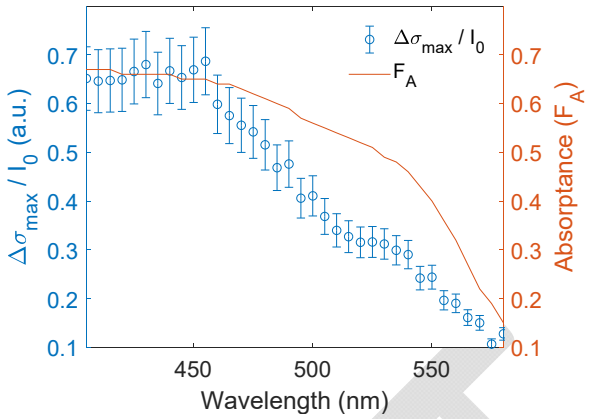

Figure 2. TRMC measurements of a 150 nm thick hematite film. (a) Photoconductivity transients normalized by the absorbed photon fluence measured by TRMC at different wavelengths. (b) Photoconductivity transients normalized by the peak photoconductivity for each wavelength. (c) Photoconductivity normalized by incident light intensity, but not absorptance (blue, left y-axis), overlayed with the absorptance F_A (orange, right y-axis) spectra.

If the $\phi \sum \mu$ product was independent of wavelength, as one would expect in conventional semiconductors such as silicon, then $\Delta\sigma_{max}/I_0$ would be proportional to the absorption spectrum, F_A. However, as shown in Figure 2(c) $\Delta\sigma_{max}/I_0$ plotted across the wavelength spectrum deviates significantly from F_A. If μ remains constant and ϕ varies with wavelength, then $\phi(\lambda) \sum \mu$ should in principle be similar to the previously calculated $\bar{p}\cdot\xi(\lambda)$ spectrum, provided that the two films have similar photogeneration yield spectra. Figure 3 compares the $\bar{p}\cdot\xi(\lambda)$ spectrum of the 7 nm hematite film (from Figure 1(c)) and the $\phi(\lambda) \sum \mu$ spectrum of the 150 nm hematite film (from Figure 2(c)), scaled by a factor so that both spectra are plotted on the same scale. Similarity between the two spectra is observed, suggesting that the two methods probe the same physical quantity and which further affirms the presented methodology to extract the shape of $\xi(\lambda)$. It also suggests that TRMC is a comparable method of probing $\xi(\lambda)$ that is not limited to ultrathin films. Variations between the spectra likely originate from the sharper features in the bulk absorption

spectrum as compared to the ultrathin film, as shown in Figure S9 in the Supplementary Information.

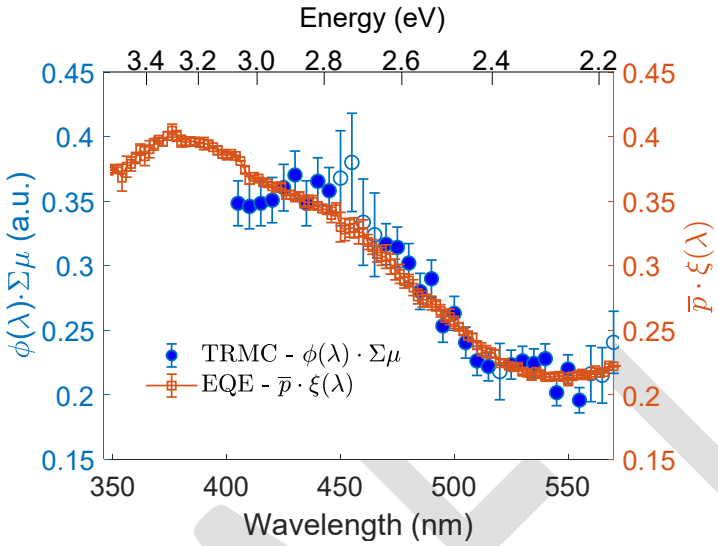

Figure 3. Comparison between the photogeneration yield spectra extracted from TRMC measurements of a thick hematite film and EQE analysis of an ultrathin hematite film. Comparison of the $\bar{p}\cdot\xi(\lambda)$ spectrum (orange squares) for an ultrathin (7 nm) hematite film photoanode and the $\phi(\lambda)\sum\mu$ spectrum (blue circles) extracted from TRMC measurements of a 150 nm thick epitaxial hematite film deposited on sapphire. The $\phi(\lambda)\sum\mu$ spectrum was scaled so as to plot the data on the same y scale. Solid markers correspond to measurements taken within an absorbed fluence range of (6-8)×10^{13} photons/cm^2/pulse. Open markers correspond to measurements taken outside this fluence range and have higher error due to the light intensity dependence.

To elucidate the contributing and non-contributing components of absorption, we multiply $\xi(\lambda)$ by $\alpha(\lambda)$ to yield the contributing absorption coefficient for generating mobile charge carriers, $\alpha_C(\lambda) = \xi(\lambda)\cdot\alpha(\lambda)$. Likewise, $[1 - \xi(\lambda)]\cdot\alpha(\lambda)$ represents the non-contributing absorption coefficient, which we denote as α_{NC}. Figure 4(a) shows the contributing and non-contributing absorption coefficients as a function of wavelength for the 7 nm thick hematite film. Since $\xi(\lambda)$ is calculated to a factor of $\bar{p}$, the absolute value of $\alpha_C(\lambda)$ cannot be extracted with an absolute certainty.

However, we can place lower and upper limits on $\alpha_C(\lambda)$ by taking $\bar{p} = 1$ (upper dotted line in Figure 4(a)) and maximal $\xi(\lambda) = 1$ (lower dotted line in Figure 4(a)), respectively. We note that qualitatively, the shape of $\alpha_C(\lambda)$ is equivalent for both cases. In the condition where $\bar{p} = 1$, this represents a "worst case" scenario for $\alpha_C(\lambda)$, as it suggests that the maximum $\xi(\lambda)$ reaches approximately 40%, and most of the absorption does not contribute to the photocurrent. Even for the best-case scenario, where maximal $\xi(\lambda) = 1$ at high excitation energies, significant losses in photogeneration are still observed throughout hematite's absorption spectrum. The real case falls somewhere between these two extremes, and hence we draw the estimated border between contributing and non-contributing absorption in Figures 4(a)-(d) as the average between the two extreme limits. The lower limit suggests a similar ratio in contributing photogeneration (~40% at 350 nm) to what was previously reported by Kennedy and Frese (~30%).[12] However, a recent report demonstrating EQE at 350 nm exceeding 75% suggests that the upper limit may be more realistic.[37] Even in the best-case scenario, $\xi(\lambda)$ is reduced by approximately half towards higher wavelengths. For the 150 nm thick hematite film, which is more representative of bulk hematite, we utilized the TRMC spectrum in Figure 3(c), and estimated absorption coefficient (see Figure S9 in the Supplementary Information), to plot in Figure 4(b) the estimated contributing and non-contributing components of its absorption. Since our TRMC data only provide the shape of the photogeneration yield spectrum, we cannot plot its lower limit as in Figure 4(a), but rather scale the average to be similar to the ultrathin-film case, indicated by the dashed dividing line in Figure 4(b). The contributing and non-contributing components of the spectrum show more structure than the ultrathin film of Figure 4(a), as may be expected from the additional features observed in the absorption coefficient spectrum of the thicker film (Figure S9), but the same general effect on $\alpha_C(\lambda)$ is observed. The upper limit was estimated by setting the maximum of the TRMC spectrum

to correspond to $\xi(\lambda)=1$, shown by the dotted line in Figure 4(b). From even this optimistic maximum, it is apparent from Figure 4(b) that above 450 nm, a significant amount of the absorbed photons are lost to non-contributing absorption in the hematite layer.

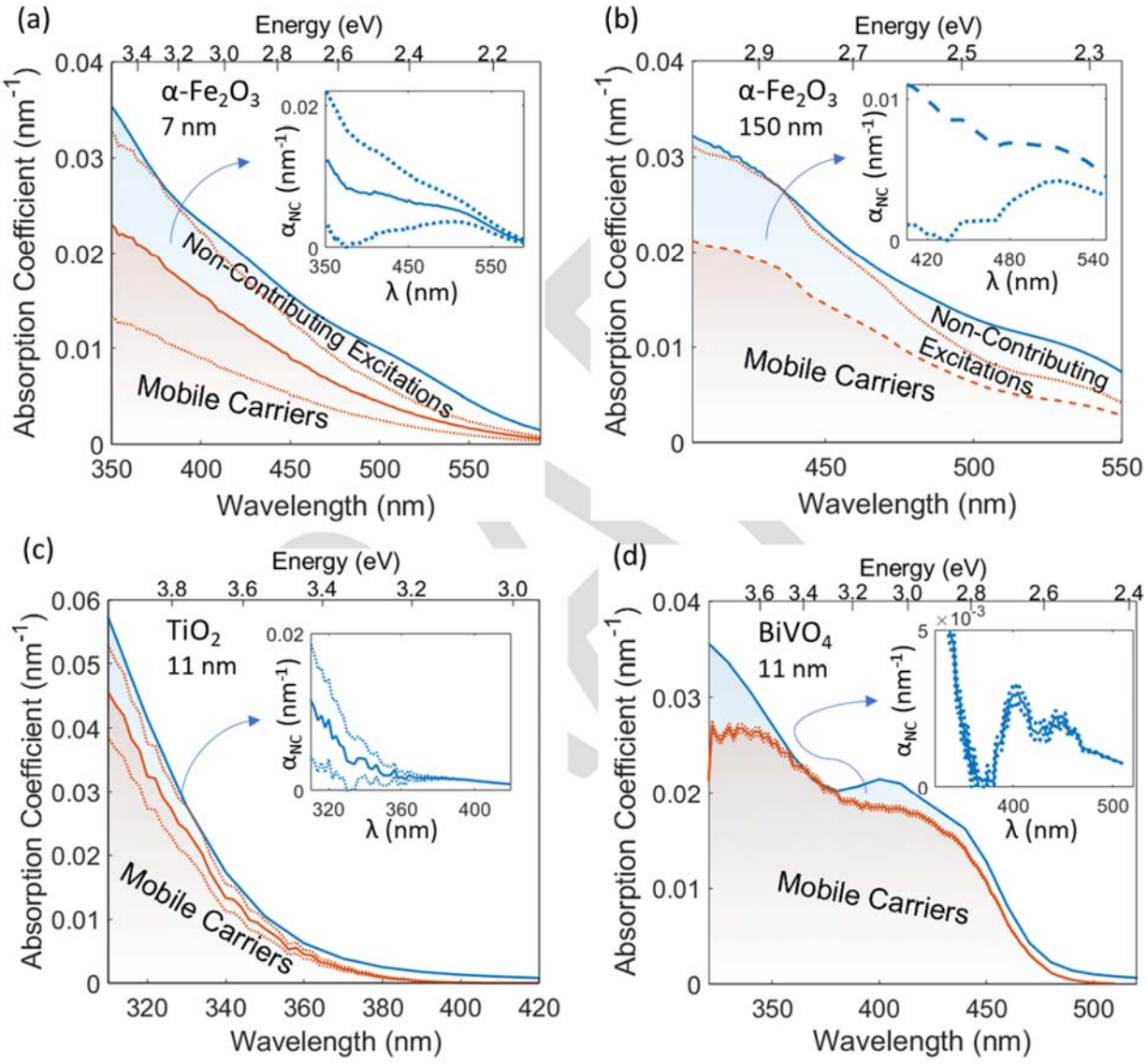

Figure 4. Contributing and non-contributing components of the absorption spectra. Absorption coefficient (α, blue curve) and average contributing absorption coefficient (α_C, orange curve) of (a) 7 nm thick hematite film; (b) estimate for 150 nm thick hematite film (described in the text); (c) 11 nm thick TiO_2 film; and (d) 11 nm thick $BiVO_4$ film. For the ultrathin film cases in panels (a), (c), and (d), the contributing absorption coefficient values were estimated from $\bar{p} \cdot \xi(\lambda)$ spectra extracted from EQE measurements by

setting lower and upper limits, where the lower limit (dashed line) corresponds to $\bar{p} = 1$ and the upper limit (dashed line) corresponds to maximal $\xi(\lambda) = 1$. The insets of (a)-(d) show the spectra of the non-contributing component, α_{NC}, corresponding to the upper blue-shaded regions in the main figures, along with upper and lower limits (dotted lines).

The salient feature in Figure 4(a) is a smooth, featureless increase of the contributing component of the absorption spectrum (α_C) with decreasing wavelength, while any subtle wavy features in the absorption spectrum (α) are a result of non-contributing absorption (α_{NC}). To inspect the non-contributing component more closely, we subtract the contributing component from the absorption spectrum and plot the result in the inset of Figure 4(a), revealing a broad peak-like feature centered around 510 nm, and a slight feature around 410 nm. This behavior is consistent with models which attribute the EQE spectrum of hematite photoelectrodes to a combination of absorption that contributes to the photocurrent and non-contributing absorption due to localized ligand field excitations.[3,12] The monotonic decrease of $\alpha_C(\lambda)$ with increasing wavelength is consistent with Hayes et al's assignment of a broad, high-energy ligand-to-metal charge transfer (LMCT) band which is responsible for mobile charge carrier generation, superimposed with non-contributing ligand field peaks at higher wavelengths.[3] This mobile tail extends to at least 620 nm (2 eV), as evident from non-zero EQE at those wavelength, shown in Figure S4. Interestingly, the non-contributing spectrum in the 150 nm thick hematite film calculated with the TRMC spectrum, shown in the inset of Figure 4(b), has a peak around 510 nm similar to the ultrathin film case, even though the absorption spectra of the two films are significantly different. Figures 4(a) and (b) together point to the existence of ligand field excitations centered at energies of approximately 2.4 and 3.0 eV (~510 and 410 nm, respectively). Complementary spectroscopic techniques such as resonant inelastic X-ray-scattering (RIXS) could

be used to verify the nature of the excitations at these energies. Further studies could clarify the role of charge carriers excited into the LMCT bands. Given the spectral agreement of the two techniques presented in this work and the lifetimes of the measured charge carriers, our results may be interpreted in the context of photogeneration into the LMCT band that have likely decayed into a longer-lived polaronic state.[17,36]

To demonstrate the applicability of our method to probe the photogeneration yield of other photoabsorber materials, we now extend the analysis to two other widely studied photoanode materials, TiO_2 (rutile) and $BiVO_4$. TiO_2 is a transition metal-oxide which has a larger bandgap (~3.0 eV) than hematite (2.0 eV),[8,38] but whose 3*d* states lie mostly in the conduction band and are also split by the crystal field. TiO_2 was the first reported photoanode material for photoelectrochemical water splitting.[39] $BiVO_4$ is a contemporary high performance photoanode material, with valence interactions between V 3*d*, O 2*p*, and Bi 6*p* states.[40] Although these materials have achieved higher IQE's than hematite, distinct signatures of polaron formation were observed.[41,42] We used the ultrathin film approach to calculate $\bar{p} \cdot \xi(\lambda)$ of these materials as for hematite, and the procedures and data for optical, EQE, and photogeneration yield calculations are presented in the Supplementary Information and Figures S10-S12. The resultant contributing and non-contributing components of the TiO_2 and $BiVO_4$ absorption spectra derived from this analysis are plotted in Figures 4(c) and 4(d), respectively, with the upper and lower limits shown as dotted lines. As expected, the extracted $\bar{p} \cdot \xi(\lambda)$ spectrum for TiO_2 (Figure S9) shows a relatively flat profile until falling to zero at the band edge, consistent with reports of unity photogeneration yield in TiO_2.[43] Thus, the upper limit for $\alpha_C(\lambda)$ shown in Figure 4(c) is very close to $\alpha(\lambda)$. For $BiVO_4$, we observe a $\bar{p} \cdot \xi(\lambda)$ spectrum with a feature that reaches a maximum of 100% at ~370 nm, where there is indication for a similar maximum in the TRMC spectrum (Figure S12). This suggests that

the charge carrier collection efficiency in this photoanode was likely close to 100% in our measurement. Interestingly, despite the much thinner film thickness and different deposition methods, the extracted photogeneration yield spectrum we obtained agrees well with the back-illumination IQE spectra of high performance undoped $BiVO_4$ photoanodes reported in Refs. [44,45], as shown in Figure S11(f). This result suggests that the upper limit for undoped $BiVO_4$ photoelectrodes may be related to the photogeneration yield of mobile charge carriers. Charge transport and recombination effects, on the other hand, are manifested in the disparity between front- and back-illumination IQE measurements in Refs. [44,45], but not for $\xi(\lambda)$. Further discussion is incorporated in the Supplementary Information. Referring to Figure 4(c), the upper limit of TiO_2 confirms a unity photogeneration yield above 360 nm, and additionally, no distinct features are observed in the non-contributing absorption spectrum suggesting the absence of localized excitations above the bandgap. It is less clear for the case of $BiVO_4$, where the analysis suggests regions of non-contributing absorption, notably below 350 nm (Figure 4(d)). The non-contributing component, plotted in the insets of Figure 4, shows no clear structure for TiO_2 (Figure 4(c)). However, the continuing non-zero absorption for wavelengths higher than 400 nm, beyond the contributing range, could indicate a long wavelength tail of absorption into localized states. $BiVO_4$, in contrast, shows distinct wavy features in both of the contributing and non-contributing components of absorption (Figure 4(d)). Such a result may be unexpected for a material whose V 3*d* states are nominally predicted to be empty, but may be related to ligand-field excitations revealed by a recent X-ray spectroscopy study, [46] which suggested some occupation of the *d*-states.

For a comparison of the practical limitations that $\xi(\lambda)$ can cause under standard solar illumination conditions, we multiplied the standard (AM1.5G) solar photon flux spectrum by the best- and worst-case $\bar{p} \cdot \xi(\lambda)$ spectra for each material, assuming a fully absorbing layer (A=1 for

all wavelengths below the absorption edge) and that all the mobile photogenerated charge carriers could be fully extracted with a collection efficiency of 100% ($p(x)$=1). In principle, this may be realized by nanostructuring[47] or resonant light trapping.[18] The results, plotted in Figure S14, show that many photons in hematite are lost to non-contributing absorption processes, even in the best-case scenario. For a numerical comparison, we calculate the ratio of contributing photons to the total amount of absorbed photons: $\%\ of\ contribuing\ photons = \frac{\int_{\lambda_{min}}^{\lambda_{max}} I_{\lambda_0}^{sun}(\lambda)\cdot\xi(\lambda)\cdot d\lambda}{\int_{\lambda_{min}}^{\lambda_{max}} I_{\lambda_0}^{sun}(\lambda)\cdot d\lambda}$, within the measured spectral range ($\lambda_{min} < \lambda < \lambda_{max}$). From the worst- and best-case estimates for $\xi(\lambda)$ of hematite, this provides a value of ~30 to 70% of the total absorbed photons between 350 and 590 nm, corresponding to a maximal photocurrent density (assuming a carrier collection efficiency of 100%) of 3.4 to 8.5 mA/cm^2 out of the total absorbed value of 12.3 mA/cm^2 in this wavelength range. This result indicates that the optical loss from non-contributing absorption processes presents a significant challenge to the viability of hematite as an efficient photoanode material. In contrast, TiO_2 and $BiVO_4$ photoanodes exhibit more efficient absorption than hematite, with a small optical loss due to non-contributing absorption over most of their maximum absorption range which covers a narrower wavelength range of the solar spectrum as shown in Figure S14.

In conclusion, we present a method to extract the photogeneration yield spectrum of mobile charge carriers from optical and EQE measurements. It is in a similar vein to IQE measurements, but crucially relies both on precise optical modelling to isolate the optical generation only in the active photoabsorber layer under operating conditions, and on having the thickness of this layer small enough so as not to be distorted by spatially-varying optical and charge transport and recombination effects. We apply this method to study an ultrathin (7 nm) hematite photoanode under *operando* photoelectrochemical conditions, and the results obtained were found consistent

for front and back illuminations and showed agreement with the photoconductivity action spectrum obtained from TRMC measurements of a thick (150 nm) hematite layer. From those results, we provide a direct link between wavelength-dependent photoelectrochemical behavior and high frequency photoconductivity measurements. We show that the photogeneration yield of mobile charge carriers provides an upper limit for the photoconversion efficiency of hematite photoanodes which is substantially lower than that predicted by its bandgap alone. Furthermore, the results are consistent with the assignment of hematite's optical absorption spectrum to a broad ligand-to-metal charge transfer (LMCT) band which generates mobile charge carriers, overlayed with non-contributing ligand field excitations. As demonstrated in this work for hematite, TiO_2 and $BiVO_4$, the proposed methodology to extract the photogeneration yield spectrum can be applied to a wide range of photoabsorber materials.

Methods

The hematite, ITO, NTO and TiO_2 depositions were performed using a turn-key PLD workstation (PLD/MBE 2100, PVD Products, USA) equipped with a KrF pulsed excimer laser beam (λ=248 nm, COMPex PRO 102 Excimer Laser, Lambda Physik / Coherent). The hematite films were deposited from a 1 cation% Sn-doped Fe_2O_3 target prepared in-house as described elsewhere.[20] The ITO current collector layer for the hematite photoanode was deposited from a commercial ITO target (purity 99.99%, In_2O_3/SnO_2 ratio of 90/10, ACI Alloys). The TiO_2 ultrathin (~10 nm) film photoanode was prepared by PLD from 1 cation% Nb-doped TiO_2 and Nb:SnO_2 (NTO) in-house made targets. For the spatial collection efficiency analysis, the hematite and ITO layers were deposited on an eagle glass substrate at a set-point temperature of 500°C and in oxygen pressure of 25 and 10 mTorr, respectively. For the TiO_2 photoanode, the NTO current collector film was

deposited at 800°C in oxygen pressure of 5 mTorr on a sapphire (0001) substrate. The Nb:doped TiO_2 film was deposited on top of the NTO film at 500°C in oxygen pressure of 25 mTorr O_2. The $BiVO_4$ photoanodes were prepared by PLD using a custom-built PLD system (PREVAC, Poland) equipped with a KrF pulsed excimer laser beam (λ=248, LPXpro 210, Coherent). For film deposition an in-house made $BiVO_4$ target was used. $BiOV_4$ films were deposited at room temperature and subsequently annealed in air at 450 °C for 2 h. Further details on the $BiVO_4$ deposition are reported elsewhere.[48]

For the TRMC measurements, a thick (~150 nm) Sn-doped hematite layer was deposited epitaxially on a sapphire (0001) substrate at a set-point substrate temperature of 800°C and in oxygen pressure of 10 mTorr as described previously in more detail.[49]

The transmission and reflection spectra of the ultrathin film hematite photoanode were measured by a Cary 5000 series UV-Vis-NIR spectrophotometer (Agilent Technologies) using a Universal Measurement Accessory (UMA). The optical parameters (complex refractive index) of the hematite, ITO, $BiVO_4$, TiO_2 and NTO layers and the glass and sapphire substrates were obtained by spectroscopic ellipsometry (VASE Ellipsometer, J.A. Woollam).

Photocurrent vs. wavelength measurements are commonly known as IPCE (Incident Photon to electron Conversion Efficiency) or EQE (External Quantum Efficiency) measurements. The EQE system we used was based on a modified Quantum Efficiency measurement kit (Oriel QE-PV-SI, Newport Inc) which included a 1 kW input Xenon lamp source with a Cornerstone 260 monochromator operated at ~ 2 nm wavelength resolution. The photocurrent was measured in 3-electrode mode using a potentiostat (Zennium, Zahner Electrik). A wavelength-calibrated 1918-C Newport optical power meter with a high-performance UV-enhanced Si-photodiode sensor was used to normalize the photocurrent by the incident light intensity. A high-power white light LED

(Mightex Systems, 6500K “glacial white” spectrum, 300 mW maximum radiant flux) was used to provide white light bias of the order of one sun intensity (1 kW/m^2) on the sample. By comparison, the monochromatic probe intensity was of the order of 10 W/m^2 . The LED bias was applied at an oblique angle either to the front or back of the sample. Care was taken to ensure proper distances, mirror angles and lateral positions of sample and detector. To overcome both current drift and fluctuation noise problems endemic for measurements under conditions of strong white light bias, an automated rotary mirror stage was implemented to alternately direct the monochromatized incident light to the sample and optical power meter, so that light current, dark current, and optical power are measured within a few seconds of each other, for each wavelength. The EQE measurements, including bias light intensity and potential dependence, are discussed in more detail in the Supplementary Information.

TRMC measurements were performed by mounting the samples in a microwave cavity cell and placing within a setup similar to the one described elsewhere.[50] A voltage controlled oscillator (SiversIMA VO3262X) generated the microwaves (X-band region, 8.4−8.7 GHz). During the measurements, a change in the microwave power ($\Delta P/P$) reflected by the cavity upon sample excitation by 3 ns (full-width at half-maximum) pulses of a wavelength tunable optical parametric oscillator (OPO) coupled to a diode-pumped Q-switched Nd:YAG laser at wavelengths between 405 and 590 nm (5 nm steps; 50 Hz repetition rate) was monitored.

Acknowledgments

D.S.E., D.A.G, and Y.P would like to acknowledge Dr. Guy Ankonina for generously assisting on technical matters whenever needed in the Technion’s Photovoltaics Laboratory, and also Alon Inbar for assisting in the EQE measurements in this work. We thank Dr. Galit Atiya for the TEM measurements, Dr. Larisa Popilevsky from the FIB Lab at the Technion’s Russell Berrie

Nanotechnology Institute (RBNI) for preparing the TEM sample, and James N. Hilfiker from J.A. Woollam Co. for helpful correspondence regarding ellipsometry analysis. The research leading to these results has received funding from the PAT Center of Research Excellence supported by the Israel Science Foundation (grant no. 1867/17). The EQE and optical measurements were carried out at the Technion's Photovoltaics Laboratory (HTRL), supported by the Russell Berrie Nanotechnology Institute (RBNI), the Nancy and Stephen Grand Technion Energy Program (GTEP) and the Adelis Foundation. Part of this research was carried out within the Helmholtz International Research School "Hybrid Integrated Systems for Conversion of Solar Energy" (HI-SCORE), an initiative co-funded by the Initiative and Networking Fund of the Helmholtz Association. Part of the work was funded by the Volkswagen Foundation. D.A.G acknowledges support from the Center for Absorption in Science at the Ministry of Aliyah and Immigrant Absorption in Israel. Y.P. acknowledges support by the Grand Technion Energy Program (GTEP), and the Levi Eshkol scholarship from the Ministry of Science and Technology of Israel. A.R. acknowledges the support of the L. Shirley Tark Chair in Science.

Contributions

D.A.G and H.D. conceived the idea and initiated the research. D.A.G, D.S.E, and Y.P. developed the methodology for the ultrathin film SCE analysis. D.A.G, Y.P., and P.S. fabricated the hematite, $BiVO_4$ and TiO_2 photoanodes. Y. P. performed the ellipsometry analysis. D.S.E designed the EQE experiment. M.K., D.F., F.F.A. and D.A.G. designed the TRMC experiments with the help of R.v.d.K. D.A.G., D.S.E, Y.P., M.K., D.F, and A.K. performed the characterizations and data analysis. D.A.G. and D.S.E. wrote the first draft of the manuscript. A.R supervised the project. All authors contributed to the scientific discussion and editing of the manuscript.

References

1. Green, M. A. Photovoltaic principles. in *Physica E: Low-Dimensional Systems and Nanostructures* **14**, 11–17 (North-Holland, 2002).

2. Liao, P. & Carter, E. A. Optical Excitations in Hematite (α-Fe2O3) via Embedded Cluster Models: A CASPT2 Study. *J. Phys. Chem. C* **115**, 20795–20805 (2011).

3. Hayes, D. *et al.* Electronic and nuclear contributions to time-resolved optical and X-ray absorption spectra of hematite and insights into photoelectrochemical performance. *Energy Environ. Sci.* **9**, 3754–3769 (2016).

4. Najafov, H., Biaggio, I., Podzorov, V., Calhoun, M. F. & Gershenson, M. E. Primary photoexcitations and the origin of the photocurrent in rubrene single crystals. *Phys. Rev. Lett.* **96**, (2006).

5. Bakulin, A. A. *et al.* The role of driving energy and delocalized states for charge separation in organic semiconductors. *Science* **335**, 1340–1344 (2012).

6. Sinkkonen, J., Ruokolainen, J., Uotila, P. & Hovinen, A. Spatial collection efficiency of a solar cell. *Appl. Phys. Lett.* **66**, 206–208 (1995).

7. Segev, G. *et al.* The Spatial Collection Efficiency of Charge Carriers in Photovoltaic and Photoelectrochemical Cells. *Joule* **2**, 210–224 (2018).

8. Sivula, K., Le Formal, F. & Grätzel, M. Solar water splitting: progress using hematite (α-Fe2O3) photoelectrodes. *ChemSusChem* **4**, 432–49 (2011).

9. Kay, A. *et al.* Effect of Doping and Excitation Wavelength on Charge Carrier Dynamics in

Hematite by Time-Resolved Microwave and Terahertz Photoconductivity. *Adv. Funct. Mater.* **30**, 1901590 (2020).

10. Hartman, J. S. & Lind, M. A. Spectral response measurements for solar cells. *Sol. Cells* **7**, 147–157 (1982).

11. Chen, Z. *et al.* Incident Photon-to-Current Efficiency and Photocurrent Spectroscopy, in *Photoelectrochemical Water Splitting: Standards, Experimental Methods, and Protocols*, edited by Z. Chen, H. N. Dinh and E. Miller, Springer (2013), pp. 87–97. doi:10.1007/978-1-4614-8298-7_7

12. Kennedy, J. H. & Frese, K. W. Photooxidation of Water at Fe2O3 Electrodes. *J. Electrochem. Soc.* **125**, 709–714 (1978).

13. Kay, A. *et al.* Wavelength Dependent Photocurrent of Hematite Photoanodes: Reassessing the Hole Collection Length. *J. Phys. Chem. C* **121**, 28287–28292 (2017).

14. Kim, D. W. *et al.* Greenlighting Photoelectrochemical Oxidation of Water by Iron Oxide. *ACS Nano* **8**, 12199–12207 (2014).

15. Su, Z., Baskin, J. S., Zhou, W., Thomas, J. M. & Zewail, A. H. Ultrafast Elemental and Oxidation-State Mapping of Hematite by 4D Electron Microscopy. *J. Am. Chem. Soc.* **139**, 4916–4922 (2017).

16. Braun, A. *et al.* Direct Observation of Two Electron Holes in a Hematite Photoanode during Photoelectrochemical Water Splitting. *J. Phys. Chem. C* **116**, 16870–16875 (2012).

17. Carneiro, L. M. *et al.* Excitation-wavelength-dependent small polaron trapping of photoexcited carriers in α-Fe2O3. *Nat. Mater.* **16**, 819–825 (2017).

18. Dotan, H. *et al.* Resonant light trapping in ultrathin films for water splitting. *Nat. Mater.* **12**, 158–64 (2013).

19. Hutter, E. M. *et al.* Direct-indirect character of the bandgap in methylammonium lead iodide perovskite. *Nat. Mater.* **16**, 115–120 (2017).

20. Piekner, Y. *et al.* Implementing Strong Interference in Ultrathin Film Top Absorbers for Tandem Solar Cells. *ACS Photonics* **5**, 5068–5078 (2018).

21. Jellison, G. E. Data analysis for spectroscopic ellipsometry. *Thin Solid Films* **234**, 416–422 (1993).

22. Sinkkonen, J., Hovinen, A., Siirtola, T., Tuominen, E. & Acerbis, M. Interpretation of the spectral response of a solar cell in terms of the spatial collection efficiency. in *Conference Record of the IEEE Photovoltaic Specialists Conference* 561–564 (IEEE, 1996). doi:10.1109/pvsc.1996.564068

23. Donolato, C. Reconstruction of the charge collection probability in a solar cell from internal quantum efficiency measurements. *J. Appl. Phys.* **89**, 5687–5695 (2001).

24. Segev, G. *et al.* Quantification of the loss mechanisms in emerging water splitting photoanodes through empirical extraction of the spatial charge collection efficiency. *Energy Environ. Sci.* **11**, 904–913 (2018).

25. Ouellette, O. *et al.* Spatial Collection in Colloidal Quantum Dot Solar Cells. *Adv. Funct. Mater.* 1908200 (2019). doi:10.1002/adfm.201908200

26. Burkhard, G. F., Hoke, E. T. & McGehee, M. D. Accounting for interference, scattering, and electrode absorption to make accurate internal quantum efficiency measurements in

organic and other thin solar cells. *Adv. Mater.* **22**, 3293–3297 (2010).

27. Fondell, M., Jacobsson, T. J., Boman, M. & Edvinsson, T. Optical quantum confinement in low dimensional hematite. *J. Mater. Chem. A* **2**, 3352–3363 (2014).

28. Chernyshova, I. V. *et al.* On the origin of an unusual dependence of (bio)chemical reactivity of ferric hydroxides on nanoparticle size. *Phys. Chem. Chem. Phys.* **12**, 14045 (2010).

29. Lin, Y., Zhou, S., Sheehan, S. W. & Wang, D. Nanonet-Based hematite heteronanostructures for efficient solar water splitting. *J. Am. Chem. Soc.* **133**, 2398–2401 (2011).

30. Riha, S. C., Devries Vermeer, M. J., Pellin, M. J., Hupp, J. T. & Martinson, A. B. F. Hematite-based photo-oxidation of water using transparent distributed current collectors. *ACS Appl. Mater. Interfaces* **5**, 360–367 (2013).

31. Barroso, M., Pendlebury, S. R., Cowan, A. J. & Durrant, J. R. Charge carrier trapping, recombination and transfer in hematite (α-Fe2O3) water splitting photoanodes. *Chemical Science* **4**, 2724–2734 (2013).

32. Savenije, T. J., Ferguson, A. J., Kopidakis, N. & Rumbles, G. Revealing the dynamics of charge carriers in polymer:fullerene blends using photoinduced time-resolved microwave conductivity. *J. Phys. Chem. C* **117**, 24085–24103 (2013).

33. Kunst, M. & Beck, G. The study of charge carrier kinetics in semiconductors by microwave conductivity measurements. *J. Appl. Phys.* **60**, 3558–3566 (1986).

34. Quist, P. A. C. *et al.* Photogeneration and decay of charge carriers in hybrid bulk heterojunctions of ZnO nanoparticles and conjugated polymers. *J. Phys. Chem. B* **110**,

10315–10321 (2006).

35. Ferguson, A. J. *et al.* Trap-limited carrier recombination in single-walled carbon nanotube heterojunctions with fullerene acceptor layers. *Phys. Rev. B - Condens. Matter Mater. Phys.* **91**, 245311 (2015).

36. Pastor, E. *et al.* In situ observation of picosecond polaron self-localisation in α-Fe2O3 photoelectrochemical cells. *Nat. Commun.* **10**, 3962 (2019).

37. Peerakiatkhajohn, P. *et al.* Stable Hematite Nanosheet Photoanodes for Enhanced Photoelectrochemical Water Splitting. *Adv. Mater.* 6405–6410 (2016). doi:10.1002/adma.201601525

38. Umebayashi, T., Yamaki, T., Itoh, H. & Asai, K. Band gap narrowing of titanium dioxide by sulfur doping. *Appl. Phys. Lett.* **81**, 454–456 (2002).

39. Fujishima, A. & Honda, K. Electrochemical photolysis of water at a semiconductor electrode. *Nature* **238**, 37–38 (1972).

40. Walsh, A., Yan, Y., Huda, M. N., Al-Jassim, M. M. & Wei, S. H. Band edge electronic structure of BiVO 4: Elucidating the role of the Bi s and V d orbitals. *Chem. Mater.* **21**, 547–551 (2009).

41. Ziwritsch, M. *et al.* Direct Time-Resolved Observation of Carrier Trapping and Polaron Conductivity in BiVO4. *ACS Energy Lett.* **1**, 888–894 (2016).

42. Elmaslmane, A. R., Watkins, M. B. & McKenna, K. P. First-Principles Modeling of Polaron Formation in TiO2 Polymorphs. *J. Chem. Theory Comput.* **14**, 3740–3751 (2018).

43. Kavan, L., Grätzel, M., Gilbert, S. E., Klemenz, C. & Scheel, H. J. Electrochemical and

photoelectrochemical investigation of single-crystal anatase. *J. Am. Chem. Soc.* **118**, 6716–6723 (1996).

44. Abdi, F. F., Firet, N. & van de Krol, R. Efficient BiVO4 Thin Film Photoanodes Modified with Cobalt Phosphate Catalyst and W-doping. *ChemCatChem* **5**, 490–496 (2013).

45. Trześniewski, B. J. *et al.* Near-complete suppression of surface losses and total internal quantum efficiency in BiVO4 photoanodes. *Energy Environ. Sci.* **10**, 1517–1529 (2017).

46. Cooper, J. K. *et al.* Electronic structure of monoclinic BiVO4. *Chem. Mater.* **26**, 5365–5373 (2014).

47. Kay, A., Cesar, I. & Grätzel, M. New benchmark for water photooxidation by nanostructured alpha-Fe2O3 films. *J. Am. Chem. Soc.* **128**, 15714–21 (2006).

48. Kölbach, M., Harbauer, K., Ellmer, K. & van de Krol, R. Elucidating the Pulsed Laser Deposition Process of BiVO4 Photoelectrodes for Solar Water Splitting. *J. Phys. Chem. C* **124**, 4438–4447 (2020).

49. Grave, D. A. *et al.* Heteroepitaxial hematite photoanodes as a model system for solar water splitting. *J. Mater. Chem. A* **4**, 3052–3060 (2016).

50. Lamers, M. *et al.* Enhanced Carrier Transport and Bandgap Reduction in Sulfur-Modified BiVO $_4$ Photoanodes. *Chem. Mater.* **30**, 8630–8638 (2018).